

Coulomb matrix elements for the impact ionization process in nanocrystals: the envelope function approach

Piotr Kowalski, Łukasz Marcinowski, Paweł Machnikowski
Institute of Physics, Wrocław University of Technology, 50-370 Wrocław, Poland
 (Dated: July 9, 2018)

We propose a method for calculating Coulomb matrix elements between exciton and biexciton states in semiconductor nanocrystals based on the envelope function formalism. We show that such a calculation requires proper treatment of the Bloch parts of the carrier wave functions which, in the leading order, leads to spin selection rules identical to those holding for optical interband transitions. Compared to the usual (intra-band) Coulomb couplings, the resulting matrix elements are additionally scaled by the ratio of the lattice constant to the nanocrystal radius. As a result, the Coulomb coupling between exciton and biexciton states scale as $1/R^2$. We present also some statistical estimates of the distribution of the coupling magnitudes and energies of the coupled states. The number of biexciton states coupled to exciton states form a certain energy range shows a power-law scaling with the ratio of the coupling magnitude to the energy separation. We estimate also the degree of mixing between exciton and biexciton states. The amount of biexciton admixture to exciton states at least 1 eV above the multiple exciton generation threshold can reach 80% but varies strongly with the nanocrystal size.

I. INTRODUCTION

Limitations of the efficiency of the existing solar cells motivate continuous search for new technological solutions that might lead to more efficient photovoltaic conversion. One of the fundamental limitations on the efficiency of the existing solar cells results from the fact that photons with energies higher than the energy gap of the semiconductor excite high energetic electrons in its conduction band. The excess energy of these charge carriers is dissipated in a phonon relaxation processes and is therefore lost for photovoltaic conversion.

Among systems that are investigated for possible use in solar energy conversion devices in order to overcome these losses are semiconductor nanocrystals (NCs). The increased efficiency of photovoltaic conversion in NC-based devices might result from multiple exciton generation (MEG) due to impact ionization (inverse Auger) processes¹. Such an effect consists in generation of two or

more electron-hole pairs by a single high energy photon and thus converts the excess above-bandgap energy into useful current. This process is enabled by Coulomb coupling between single-pair (exciton, X) states and two-pair (biexciton, BX) states in a NC (or, in general, between states with n and $n + 1$ pairs), as shown in Fig. 1. It can result from the system dynamics after optical creation of a single electron-hole pair, during which an electron relaxes within the conduction band transferring its energy to an intraband excitation (an inverse Auger process, in which the two situations in Fig. 1 are understood as “initial” and “final”). However, very short time scales of the biexciton generation² suggest that the process may be instantaneous and result from the mixing between the X and BX states. In this case, the original X states contain on the average more than one electron-hole pair, while the initially dark BX states become optically active. The MEG process can be thus understood as an excitation of a BX state mediated by a “virtual” X state to which it is coupled² (the two states in Fig. 1 are then interpreted as the “virtual” state that is directly coupled to light and the final BX state that is optically excited via the Coulomb-induced mixing). Clearly, in this picture, the degree of mixing between the states and their spectral distributions (spectral densities) are crucial for the efficiency of the MEG process. Another possible process³ involves Coulomb coupling between empty NC and BX states and relies on an intermediate BX state.

The MEG effect has been observed using a variety of experimental techniques in NCs formed of various narrow-gap semiconductors and under various excitation conditions^{2,4-9}, as well as in systems of coupled NCs¹⁰. In some experiments, quantum efficiencies as high as 700% were observed¹¹. On the other hand, some later experimental investigation showed much lower efficiencies of the MEG process or even no traces of MEG at all¹²⁻¹⁶. The subsequent discussion of the experimental factors involved in extracting the MEG efficiency from

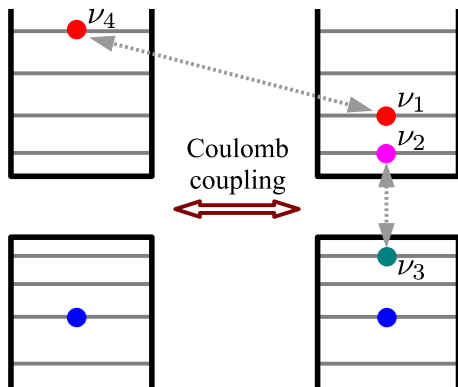


FIG. 1: Schematic representation of the impact ionization process in a nanocrystal. The state labels refer to labeling of the matrix elements derived in Sec. II.

experimental data^{17–19} showed that performing reliable experiments and correctly interpreting their results is not quite trivial. Uncontrolled effects present in the experiments, like photocharging of the NC core and charge trapping at the surface ligands, can indeed lead to a considerably overestimated result¹⁹. In any case, however, enhanced photocurrent due to MEG has been observed in real NC-based solar cells^{20,21} providing a direct proof of the usefulness of this process in solar energy conversion. Still, the experimental results and the controversies they arouse motivate theoretical work aimed at full understanding of the MEG process in NCs.

Theoretical description of the X and BX spectrum and the X-BX couplings is sought within various approaches available for modeling semiconductor nanostructures. Atomistic approaches to this problem include density functional theory^{22,23}, pseudopotential^{24–27} and tight binding^{28–30} methods. However, the high computational complexity of atomistic methods limits the size of tractable systems and forces one to radically truncate the basis of single particle functions when computing the properties of few-particle complexes. Therefore, one often resorts to an envelope function approach based on the k-p theory^{31–33}, which was very useful in the past for understanding the fundamental electronic properties of NCs³⁴. Apart from establishing the spectral distribution of the X and BX levels, the central point of any theoretical modeling of the MEG process is the evaluation of the X-BX Coulomb matrix element which can then be used, e.g. to find the spectral properties of correlated X-BX states³⁵ or to study the system kinetics^{31,32,35–38}.

In the present paper, we present the calculations of the Coulomb matrix elements between X and BX states within an envelope function approach. This approach is much more explicit than the atomistic computations and yields relatively transparent formulas for the matrix elements that offer much more insight into the properties of the X-BX couplings. This allows us to point out that the correct treatment of the Bloch parts of the carrier wave functions (which was not made explicit in previous works) leads to selection rules for the newly created pair identical to those holding for optical transitions. In addition, the interband character of the coupling reduces the matrix element (as compared to the usual electron-electron interaction) by a factor a/R , where a is on the order of the lattice constant and R is the radius of the NC, and leads to the $1/R^2$ dependence on the NC size. On the practical side, the envelope function approach leads to formulas that, for a spherical NC, can be evaluated at very modest computational cost. This allows us to find coupled pairs of X-BX states in a very broad energy window and to study the distribution of the magnitudes of the matrix elements vs. the energies of the coupled configurations. Here, we restrict ourselves to the simplest example of an application of the proposed formalism and calculate the matrix elements using a very simple model of wave functions in order to extract very general statistics on the X-BX couplings. The important

conclusion from this study is that the X-BX state mixing is on the average dominated by relatively strongly coupled pairs of energetically close states. This means, on one hand, that admixture of the BX states to the X states (or conversely) cannot be treated perturbatively. On the other hand, it shows that truncating the set of states to an energy window around a given X (or BX) state is a well-defined and convergent approximation. Quantitatively, the matrix elements found for an InAs NC are in the meV range, which is clearly very small compared to typical separations of single particle states in these structures. Still, admixture of BX states to a given X state can reach several to a few tens per cent due to relatively large density of coupled BX states.

The paper is organized as follows. In Sec. II, we derive general formulas for the Coulomb matrix element between X and BX configurations in a spherical NC. Next, in Sec. III we present a simple example of an application of this formalism. Sec. IV contains results on the statistical distribution of the X-BX couplings and an estimate of the degree of X-BX mixing. Sec. V contains concluding discussion of the results and the outlook for their extension.

II. MODEL AND GENERAL DESCRIPTION

In this section we present a general derivation of the matrix element underlying the MEG process in a NC. The calculation will be performed in the envelope function approximation. To simplify the notation we assume identical envelopes for all bands but generalization to arbitrary envelope wave functions is straightforward.

A. General considerations

We calculate the matrix elements between single-subband wave functions. The result can be generalized to derive the Coulomb couplings between states in more accurate models including band mixing. We consider a spherical NC of radius R with the dielectric constant ϵ_s , emerged in a host material with the dielectric constant ϵ_h . The electron-trion coupling responsible for the impact ionization process results from the Coulomb coupling between the states in conduction and valence bands, corresponding to an intraband transition of an electron accompanied by the creation of an additional electron-hole pair (inverse Auger process) as shown schematically in Fig.1. The relevant part of the Coulomb Hamiltonian is

$$H = \sum_{\nu_1 \nu_2 \nu_3 \nu_4} \sum_{\lambda \sigma_1 \sigma_2 \sigma_4} h_{\nu_1 \nu_2 \nu_3 \nu_4}^{(\sigma_1 \sigma_2 \lambda \sigma_4)} a_{\sigma_1 \nu_1}^\dagger a_{\sigma_2 \nu_2}^\dagger a_{\lambda \nu_3} a_{\sigma_4 \nu_4} + \text{H.c.},$$

where $a_{\sigma_i \nu_i}$, $a_{\sigma_i \nu_i}^\dagger$ are the annihilation and creation operators for an electron in the conduction subband σ_i and in the envelope state ν_i , while $a_{\lambda \nu_i}$, $a_{\lambda \nu_i}^\dagger$ are the annihilation and creation operators for an electron in the valence

subband λ and in the envelope state ν . The index ν_i represents the whole set of relevant quantum numbers. The graphical interpretation of this term is given in Fig. 1. We write the wave functions in the single-band envelope approximation in the form $\Psi_{\sigma\nu}(\mathbf{r}, s) = \psi_\nu(\mathbf{r})u_\sigma(\mathbf{r}, s)$, where $\psi_\nu(\mathbf{r})$ is the envelope and $u_\sigma(\mathbf{r}, s)$ is the lattice-periodic Bloch part (s denotes the value of the electron spin). The position vector is written as $\mathbf{r} = \mathbf{r}_i + \boldsymbol{\xi}$, where \mathbf{r}_i denotes the center of the i th unit cell (u.c.) and $\boldsymbol{\xi}$ lies in the first u.c. The integration over the whole NC volume is then expressed as a summation over all the unit cells and integration over one cell. We assume that the envelope functions change slowly, so that $\psi_\nu(\mathbf{r}_i + \boldsymbol{\xi}) \approx \psi_\nu(\mathbf{r}_i)$ and use the periodicity of the Bloch functions $u_\sigma(\mathbf{r}_i + \boldsymbol{\xi}) = u_\sigma(\boldsymbol{\xi})$. The matrix element is then given by

$$h_{\nu_1\nu_2\nu_3\nu_4}^{(\sigma_1\sigma_2\lambda\sigma_4)} = \sum_{ss'} \sum_{ij} \int_{\text{u.c.}} d^3\xi \int_{\text{u.c.}} d^3\xi' \quad (1)$$

$$\times \psi_{\nu_1}^*(\mathbf{r}_j) u_{\sigma_1}^*(\boldsymbol{\xi}', s') \psi_{\nu_2}^*(\mathbf{r}_i) u_{\sigma_2}^*(\boldsymbol{\xi}, s) U(\mathbf{r}_i + \boldsymbol{\xi}, \mathbf{r}_j + \boldsymbol{\xi}') \\ \times \psi_{\nu_3}(\mathbf{r}_i) u_\lambda(\boldsymbol{\xi}, s) \psi_{\nu_4}(\mathbf{r}_j) u_{\sigma_4}(\boldsymbol{\xi}', s').$$

The two-particle interaction energy in a spherical NC is composed of the direct Coulomb interaction and the coupling via surface polarization due to dielectric discontinuity between the NC and the environment³⁹, $U(\mathbf{r}, \mathbf{r}') = U_{\text{direct}}(\mathbf{r}, \mathbf{r}') + U_{\text{pol}}(\mathbf{r}, \mathbf{r}')$, where

$$U_{\text{direct}}(\mathbf{r}, \mathbf{r}') = \frac{e^2}{4\pi\epsilon_0\epsilon_s} \frac{1}{|\mathbf{r} - \mathbf{r}'|},$$

$$U_{\text{pol}}(\mathbf{r}, \mathbf{r}') = -\frac{e^2}{4\pi\epsilon_0\epsilon_s} \sum_k \alpha_k \frac{(rr')^k}{R^{2k+1}} P_k(\cos\gamma).$$

Here $\cos\gamma = \mathbf{r} \cdot \mathbf{r}' / (rr')$, P_k are Legendre polynomials, $\chi_k = (k+1)(\epsilon-1)/(k\epsilon+k+1)$ with $\epsilon = \epsilon_s/\epsilon_h$, and we take into account only the two-particle part of the surface polarization term.

In consequence, the Coulomb matrix element splits into the corresponding two contributions

$$h_{\nu_1\nu_2\nu_3\nu_4}^{(\sigma_1\sigma_2\lambda\sigma_4)} = h_{\nu_1\nu_2\nu_3\nu_4}^{(\sigma_1\sigma_2\lambda\sigma_4, \text{dir})} + h_{\nu_1\nu_2\nu_3\nu_4}^{(\sigma_1\sigma_2\lambda\sigma_4, \text{pol})}. \quad (2)$$

B. Direct Coulomb coupling

For the direct Coulomb term, which is singular at $\mathbf{r} = \mathbf{r}'$, we split the summation into $i = j$ (short-range contribution) and $i \neq j$ (long range contribution). For the former, we use the expansion⁴⁰

$$\frac{1}{|\boldsymbol{\xi} - \boldsymbol{\xi}'|} = \sum_{l=0}^{\infty} \frac{\xi_{<}^l}{\xi_{>}^{l+1}} \sum_{m=-l}^l \frac{4\pi}{2l+1} Y_{lm}^*(\theta'\phi') Y_{lm}(\theta, \phi), \quad (3)$$

where $\xi_{<} = \min(\xi, \xi')$, $\xi_{>} = \max(\xi, \xi')$, θ, ϕ and θ, ϕ' are the spherical coordinates of the vectors $\boldsymbol{\xi}$ and $\boldsymbol{\xi}'$, respectively, and $Y_{lm}(\theta, \phi)$ are spherical harmonics. Since both σ_1 and σ_4 correspond to s -type conduction band states only the term with $l = 0$ is non-zero in the integral over

$\boldsymbol{\xi}'$ when Eq. (3) is substituted to Eq. (1). This term, however, yields a vanishing integral over $\boldsymbol{\xi}$, as λ and σ_3 correspond to states with p and s symmetries, respectively. Hence, the short-range contribution vanishes.

In the long range term, we expand $|\mathbf{r}_i + \boldsymbol{\xi} - \mathbf{r}_j - \boldsymbol{\xi}'|^{-1}$ to the linear order in $(\boldsymbol{\xi} - \boldsymbol{\xi}')$. The summation over i, j in Eq. (1) is then replaced by integration, where one formally excludes a small volume around $\mathbf{r} = \mathbf{r}'$ (which is represented by a prime over an integral)⁴¹. Thus one finds in the leading order

$$h_{\nu_1\nu_2\nu_3\nu_4}^{(\sigma_1\sigma_2\lambda\sigma_4, \text{dir})} = \frac{e^2}{4\pi\epsilon_0\epsilon_s} \sum_{ss'} \frac{1}{V^2} \quad (4)$$

$$\times \int d^3r \int' d^3r' \psi_{\nu_1}^*(\mathbf{r}') \psi_{\nu_2}^*(\mathbf{r}) \nabla \frac{1}{|\mathbf{r} - \mathbf{r}'|} \psi_{\nu_3}(\mathbf{r}) \psi_{\nu_4}(\mathbf{r}') \\ \times \int d^3\xi' u_{\sigma_1}^*(\boldsymbol{\xi}', s') u_{\sigma_4}(\boldsymbol{\xi}', s') \int d^3\xi u_{\sigma_2}^*(\boldsymbol{\xi}, s) \boldsymbol{\xi} u_\lambda(\boldsymbol{\xi}, s),$$

where V is the volume of the unit cell. The zeroth order term as well as the term containing $\boldsymbol{\xi}'$ vanish because the functions u_{σ_1} and u_{σ_4} both have s -type symmetry. The integration over \mathbf{r}' can be extended onto the whole space because the singularity of $\nabla(1/r)$ is integrable in three dimensions. Using the orthogonality of Bloch functions and the definition

$$\sum_s \int d^3\xi u_{\sigma_2}^*(\boldsymbol{\xi}, s) \boldsymbol{\xi} u_\lambda(\boldsymbol{\xi}, s) = V \mathbf{a}_{\sigma_2\lambda}, \quad (5)$$

one then finds

$$h_{\nu_1\nu_2\nu_3\nu_4}^{(\sigma_1\sigma_2\lambda\sigma_4, \text{dir})} = -\frac{i}{(2\pi)^3} \frac{e^2}{\epsilon_0\epsilon_s} \int d^3q \frac{\mathbf{q} \cdot \mathbf{a}_{\sigma_2\lambda}}{q^2} \quad (6)$$

$$\times \mathcal{F}_{\nu_1\nu_4}(\mathbf{q}) \mathcal{F}_{\nu_3\nu_2}^*(\mathbf{q}) \delta_{\sigma_1\sigma_4},$$

where we used the identity

$$\nabla \frac{1}{|\mathbf{r} - \mathbf{r}'|} = -\frac{i}{2\pi^2} \int d^3q \frac{\mathbf{q}}{q^2} e^{i\mathbf{q} \cdot (\mathbf{r}' - \mathbf{r})},$$

and the form-factors are defined as

$$\mathcal{F}_{\nu\nu'}(\mathbf{q}) = \int d^3r \psi_\nu^*(\mathbf{r}) e^{i\mathbf{q} \cdot \mathbf{r}} \psi_{\nu'}(\mathbf{r}). \quad (7)$$

Note that, according to Eq. (6), the leading order term in the matrix element responsible for the MEG (impact ionization) process involves $\nabla(\mathbf{r} - \mathbf{r}')^{-1}$ (as opposed to just $(\mathbf{r} - \mathbf{r}')^{-1}$ in an intraband matrix element), hence the resulting quantity is proportional to $1/R^2$. This is a consequence of the orthogonality of the Bloch functions that leads to the appearance of the bulk interband matrix element of the position operator, $\mathbf{a}_{\sigma_2\lambda}$, (which obviously has the dimension of length) in the interband Coulomb term. Note that the resulting selection rules for the impact ionization process are the same as for the dipole-allowed optical transitions.

In a crystal with zinc-blende structure, the topmost valence band corresponds to the $3/2$ band angular momentum. The non-zero matrix elements $\mathbf{a}_{\sigma\lambda}$ between

the four valence bands with $\lambda = \pm 1/2, \pm 3/2$ and the two conduction bands with $\sigma = \pm 1/2$ are

$$\mathbf{a}_{\pm\frac{1}{2}, \pm\frac{3}{2}} = \sqrt{3} \mathbf{a}_{\mp\frac{1}{2}, \pm\frac{1}{2}} = \frac{a_0}{\sqrt{2}} \begin{pmatrix} \mp 1 \\ -i \\ 0 \end{pmatrix}, \quad (8a)$$

$$\mathbf{a}_{\pm\frac{1}{2}, \pm\frac{1}{2}} = a_0 \sqrt{\frac{2}{3}} \begin{pmatrix} 0 \\ 0 \\ 1 \end{pmatrix}, \quad (8b)$$

where a_0 is a bulk material constant. Hence, we find

$$\mathbf{q} \cdot \mathbf{a}_{\sigma_2, \lambda} = \alpha_{\sigma_2 \lambda} q a_0 \sqrt{\frac{4\pi}{3}} Y_{1, \Delta m}(\vartheta, \varphi), \quad (9)$$

where $\Delta m = \lambda - \sigma_2$ and the non-zero coefficients are

$$\alpha_{\pm\frac{1}{2}, \pm\frac{3}{2}} = 1, \quad \alpha_{\mp\frac{1}{2}, \pm\frac{1}{2}} = \frac{1}{\sqrt{3}}, \quad \alpha_{\pm\frac{1}{2}, \pm\frac{1}{2}} = \sqrt{\frac{2}{3}}.$$

C. Surface polarization contribution

The surface polarization term is smooth, therefore separation into short-range and long-range parts is not necessary. Again, we expand the potential into the Taylor series in $\boldsymbol{\xi}, \boldsymbol{\xi}'$,

$$U_{\text{pol}}(\mathbf{r}_i + \boldsymbol{\xi}, \mathbf{r}_j + \boldsymbol{\xi}') \approx U_{\text{pol}}(\mathbf{r}_i, \mathbf{r}_j) + \boldsymbol{\xi} \cdot \nabla_i U_{\text{pol}}(\mathbf{r}_i, \mathbf{r}_j) + \boldsymbol{\xi}' \cdot \nabla_j U_{\text{pol}}(\mathbf{r}_i, \mathbf{r}_j) + \dots,$$

and keep only the lowest order non-vanishing term. The first and third terms in the above expression lead to vanishing integrals in Eq. (1) because of the orthogonality of the Bloch functions for different bands. Using the properties of Legendre polynomials and the addition theorem for spherical harmonics⁴⁰ we find for the second term

$$\begin{aligned} \boldsymbol{\xi} \cdot \nabla_i U_{\text{pol}}(\mathbf{r}_i, \mathbf{r}_j) &= \frac{e^2}{\epsilon_0 \epsilon_s R} \sum_k \frac{r_i^{k-1} r_j^k}{R^{2k}} \\ &\times \left[\frac{\boldsymbol{\xi} \cdot \mathbf{r}_i}{r_i} \sum_{\substack{l < k \\ l-k \text{ even}}} \sum_{m=-l}^l Y_{lm}^*(\theta_i, \phi_i) Y_{lm}(\theta_j, \phi_j) \right. \\ &\left. - \frac{\boldsymbol{\xi} \cdot \mathbf{r}_j}{r_j} \sum_{\substack{l < k \\ l-k \text{ odd}}} \sum_{m=-l}^l Y_{lm}^*(\theta_i, \phi_i) Y_{lm}(\theta_j, \phi_j) \right], \end{aligned}$$

where (r_i, θ_i, ϕ_i) are the spherical coordinates of the vector \mathbf{r}_i . One substitutes the resulting expression into Eq. (1), performs the integration over the Bloch functions according to Eq. (5) and changes the summation over i, j into integration as previously. As a result, the surface polarization contribution to the matrix element is

$$h_{\nu_1 \nu_2 \nu_3 \nu_4}^{(\sigma_1 \sigma_2 \lambda \sigma_4, \text{pol})} = h_{\nu_1 \nu_2 \nu_3 \nu_4}^{(\sigma_1 \sigma_2 \lambda \sigma_4, \text{pol}-1)} + h_{\nu_1 \nu_2 \nu_3 \nu_4}^{(\sigma_1 \sigma_2 \lambda \sigma_4, \text{pol}-2)},$$

where

$$\begin{aligned} h_{\nu_1 \nu_2 \nu_3 \nu_4}^{(\sigma_1 \sigma_2 \lambda \sigma_4, \text{pol}-j)} &= \quad (10) \\ &(-1)^{j-1} \frac{e^2}{\epsilon_0 \epsilon_s R} \sum_k \chi_k \int d^3 r_1 \int d^3 r_2 \psi_{\nu_1}^*(\mathbf{r}_2) \psi_{\nu_2}^*(\mathbf{r}_1) \\ &\times \frac{r_1^{k-1} r_2^k}{R^{2k}} \frac{\mathbf{a}_{\sigma_2 \lambda} \cdot \mathbf{r}_j}{r_j} \sum_{\substack{l < k \\ l-k+j \text{ odd}}} \sum_{m=-l}^l Y_{lm}^*(\theta_1, \phi_1) \\ &\times Y_{lm}(\theta_2, \phi_2) \psi_{\nu_3}(\mathbf{r}_1) \psi_{\nu_4}(\mathbf{r}_2) \delta_{\sigma_1, \sigma_4} \end{aligned}$$

for $j = 1, 2$.

As previously, using Eq. (8a) and Eq. (8b), one finds

$$\mathbf{r} \cdot \mathbf{a}_{\sigma_2, \lambda} = \alpha_{\sigma_2 \lambda} r a_0 \sqrt{\frac{4\pi}{3}} Y_{1, \Delta m}(\theta, \phi). \quad (11)$$

From Eq. (11), again the general scaling of the matrix element as $1/R^2$ follows.

D. Coulomb coupling between two- and four-particle configurations

Assuming that the NC is spherical and neglecting the spin-orbit coupling, the total spins of electrons and holes are separately good quantum numbers. The bright states involving the hole in a state with $\pm 3/2$ angular momentum will be denoted by $|\alpha\beta \uparrow\downarrow\rangle$ and $|\alpha\beta \downarrow\uparrow\rangle$, where α and β denote the electron and hole states (representing the relevant sets of quantum numbers) and the arrows represent the values of the projection of the band angular momentum of the electron and hole on the selected quantization axis. The states with dark spin configurations as well as the states involving a hole with $\pm 1/2$ band angular momentum (represented by \uparrow, \downarrow) are denoted in an analogous way. Note that, e.g., \uparrow denotes hole spin $+3/2$, which results from a transition from the $\lambda = -3/2$ valence band.

The four-particle states are labeled by the electron spin configuration $(S, T_{\pm, 0})$ for singlet and the three triplet states, respectively and by the hole spin configuration. If only the topmost valence band ($j = 3/2$) is included than the two-hole configurations can be classified in the following way, which is convenient for our purpose: The states with both holes in $\pm 3/2$ or both holes in $\pm 1/2$ states are combined in singlet-like and triplet-like configurations $S^{3/2}, T_{\pm, 0}^{3/2}$ and $S^{1/2}, T_{\pm, 0}^{1/2}$. For instance, in terms of the hole creation operators $\hat{h}_{\mu, \lambda}^\dagger$, the two-hole state with $S^{3/2}$ and $T_0^{3/2}$ spin configurations is $|\mu\mu'\Sigma_h\rangle = (\eta_{\mu\mu'}/\sqrt{2})(\hat{h}_{\mu\uparrow}^\dagger \hat{h}_{\mu'\downarrow}^\dagger \pm \hat{h}_{\mu'\uparrow}^\dagger \hat{h}_{\mu\downarrow}^\dagger)|0\rangle$, where $\mu \geq \mu'$ (equality allowed only in the singlet configuration) and $\eta_{\mu\mu'} = 1/\sqrt{2}$ for $\mu = \mu'$, and $\eta_{\mu\mu'} = 1$ otherwise. While these spin configurations are not total spin eigenstates, they have a definite parity under particle permutation, implying also a definite (opposite) parity of the orbital wave

functions. Hence, the resulting states automatically diagonalize the hole exchange interaction. The spin configurations with one hole in a $\pm 3/2$ state and one hole in the $\pm 1/2$ state are obtained simply by symmetrizing (S) or antisymmetrizing (A) the corresponding two-hole states with respect to the orbital wave functions. For instance, $|\mu\mu', S_{\uparrow\downarrow}\rangle = (\eta_{\mu\mu'}/\sqrt{2})(\hat{h}_{\mu\uparrow}^\dagger\hat{h}_{\mu'\downarrow}^\dagger + \hat{h}_{\mu'\uparrow}^\dagger\hat{h}_{\mu\downarrow}^\dagger)|0\rangle$, $\mu \geq \mu'$, and $|\mu\mu', A_{\uparrow\downarrow}\rangle = (\eta_{\mu\mu'}/\sqrt{2})(\hat{h}_{\mu\uparrow}^\dagger\hat{h}_{\mu'\downarrow}^\dagger - \hat{h}_{\mu'\uparrow}^\dagger\hat{h}_{\mu\downarrow}^\dagger)|0\rangle$, $\mu > \mu'$. The four-particle (biexciton) states are then labeled by $|\nu\nu'\Sigma_e; \mu\mu'\Sigma_h\rangle$, where ν, ν' denote electron states, μ, μ' are hole states, and Σ_e, Σ_h represent spin configurations.

The couplings between the two-particle and four-particle configurations, which are responsible for the impact ionization process, are then expressed in terms of the Coulomb matrix elements given by Eqs. (6) and (10). For instance, the non-zero couplings between the four-particle states with both holes in the spin- $\pm 3/2$ states and the two-particle state $|\alpha\beta \uparrow\downarrow\rangle$ are (denoting $h_{\Sigma_e\Sigma_h} = \langle \nu\nu'\Sigma_e, \mu\mu'\Sigma_h | H | \alpha\beta \uparrow\downarrow \rangle$)

$$\begin{aligned} h_{SS^{3/2}} &= \frac{\eta_{\nu\nu'}\eta_{\mu\mu'}}{2} [\delta_{\mu\beta} (h_1 + h_2) + \delta_{\mu'\beta} (h_3 + h_4)], \\ h_{ST_0^{3/2}} &= \frac{\eta_{\nu\nu'}}{2} [\delta_{\mu\beta} (-h_1 - h_2) + \delta_{\mu'\beta} (h_3 + h_4)], \\ h_{T_0S^{3/2}} &= \frac{\eta_{\mu\mu'}}{2} [\delta_{\mu\beta} (h_1 - h_2) + \delta_{\mu'\beta} (h_3 - h_4)], \\ h_{T_0T_0^{3/2}} &= \frac{1}{2} [\delta_{\mu\beta} (-h_1 + h_2) + \delta_{\mu'\beta} (h_3 - h_4)], \\ h_{T_+T_-^{3/2}} &= \delta_{\mu\beta} (-h'_1 + h'_2) + \delta_{\mu'\beta} (h'_3 - h'_4), \end{aligned}$$

where $h_1 = h_{\nu\nu'\mu'\alpha}^{(\uparrow\downarrow\uparrow\uparrow)}$, $h_2 = h_{\nu'\nu\mu'\alpha}^{(\uparrow\downarrow\uparrow\uparrow)}$, $h_3 = h_{\nu\nu'\mu\alpha}^{(\uparrow\downarrow\uparrow\uparrow)}$, $h_4 = h_{\nu'\nu\mu\alpha}^{(\uparrow\downarrow\uparrow\uparrow)}$, $h'_1 = h_{\nu\nu'\mu'\alpha}^{(\uparrow\uparrow\downarrow\uparrow)}$, $h'_2 = h_{\nu'\nu\mu'\alpha}^{(\uparrow\uparrow\downarrow\uparrow)}$, $h'_3 = h_{\nu\nu'\mu\alpha}^{(\uparrow\uparrow\downarrow\uparrow)}$, $h'_4 = h_{\nu'\nu\mu\alpha}^{(\uparrow\uparrow\downarrow\uparrow)}$. Since one of the holes is a spectator in the impact ionization process and its state is conserved there is no coupling between this two-particle state and any state with both holes in a $\pm 1/2$ spin state. The results for the state $|\alpha\beta \downarrow\uparrow\rangle$ are obtained by flipping all the spins and the couplings for a two-particle state with a hole in a $\pm 1/2$ state are easily derived by exchanging the role of the $\pm 3/2$ and $\pm 1/2$ hole spins.

With similar notation as above and $\lambda = \uparrow, \downarrow$, the non-vanishing couplings between four-particle states with one hole in a $\pm 1/2$ state and one in a $\pm 3/2$ state and the same two-particle state are

$$\begin{aligned} h_{SS_{\lambda\downarrow}} &= \frac{\eta_{\nu\nu'}\eta_{\mu\mu'}}{2} [\delta_{\mu\beta} (h''_1 + h''_2) + \delta_{\mu'\beta} (h''_3 + h''_4)], \\ h_{SA_{\lambda\downarrow}} &= \frac{\eta_{\nu\nu'}}{2} [-\delta_{\mu\beta} (h''_1 + h''_2) + \delta_{\mu'\beta} (h''_3 + h''_4)], \\ h_{T_0S_{\lambda\downarrow}} &= \frac{\eta_{\mu\mu'}}{2} [\delta_{\mu\beta} (h''_1 - h''_2) + \delta_{\mu'\beta} (h''_3 - h''_4)], \\ h_{T_0A_{\lambda\downarrow}} &= \frac{1}{2} [\delta_{\mu\beta} (-h''_1 + h''_2) + \delta_{\mu'\beta} (h''_3 - h''_4)], \\ h_{T_+S_{\lambda\downarrow}} &= \frac{\eta_{\mu\mu'}}{\sqrt{2}} [\delta_{\mu\beta} (h'''_1 - h'''_2) + \delta_{\mu'\beta} (h'''_3 - h'''_4)], \\ h_{T_+A_{\lambda\downarrow}} &= \frac{1}{\sqrt{2}} [\delta_{\mu\beta} (-h'''_1 + h'''_2) + \delta_{\mu'\beta} (h'''_3 - h'''_4)], \end{aligned}$$

where h''_i and h'''_i are defined as h_i and h'_i , respectively, but with the third spin (upper) index replaced by λ . Again, the results for the two-particle state $|\alpha\beta \downarrow\uparrow\rangle$ are obtained by flipping all the spins.

Thus, we have characterized the Coulomb couplings between two-particle and four-particle configurations within the envelope function approach. The matrix elements for transitions between various subbands can be used in a calculation of couplings in an arbitrary envelope function model, including the common one based on an 8-band $k \cdot p$ Hamiltonian (obviously, the classification of the four-particle configuration must then be extended to account for the spin-orbit coupling). This rather complex task is beyond the scope of this paper. In the following section, we limit ourselves to the simplest application of the results obtained above to a single-band model.

III. MATRIX ELEMENT FOR A SIMPLE MODEL OF NANOCRYSTAL WAVE FUNCTIONS

In this section, as the simplest example of an application of the general envelope function formalism of Sec. II, we find the Coulomb matrix elements between the 2- and 4-particle states assuming simple single-band carrier wave functions. While perhaps not quantitatively accurate, this calculation yields a useful estimate of the overall magnitude of the couplings and of the resulting degree of mixing between two- and four-particle configurations as well as some statistics of the coupling strengths that, taken globally, may be close to the actual ones. Below, we define the simple model of wave functions which is then used to implement the general findings of the previous section.

A. Model of the wave functions

An InAs NC is modeled as a spherical potential well of radius R with infinite potential walls. The envelope wave function is given by

$$\psi_\nu(\mathbf{r}) = \frac{1}{R^{3/2}} N_{nl} Y_{lm}(\theta, \phi) j_l(x_{ln} r/R), \quad (12)$$

where we write explicitly $\nu = (nlm)$, x_{ln} is the n th zero of the spherical Bessel function j_l and $N_{nl} = \sqrt{2}/|j_{l+1}(x_{ln})|$. In our model, we neglect band mixing and include the Coulomb interaction between electrons and holes in the lowest order only.

The corresponding energy levels for electrons and holes are $E_{nl}^{(e,h)} = \hbar^2 x_{ln}^2 / (2m_{e,h}^* R^2)$. We take the heavy hole effective mass $m_h^* = 0.35m_0$, where m_0 is the free electron mass, and use the implicit formula for the energy-dependent electron mass in the decoupled bands approximation³⁴ $m_e^* = m_0[\alpha + E_P/(E_g + E_{nl})]^{-1}$, where $E_P = 22.2$ eV, $E_g = 0.418$ eV is the bulk band gap, and the parameter $\alpha = 0.77$ accounts for the coupling to higher bands. Using the implicit formula for the electron

and a constant effective mass for the hole is motivated by the small effective mass of the former which leads to larger kinetic energies as compared to the hole.

In the energy levels of the few-particle states, we include the lowest order corrections due to Coulomb interactions, including the surface polarization terms³⁹. In the energies of the four-particle states also exchange interactions are taken into account.

B. Direct Coulomb coupling

In Eq. (7), we substitute the wave functions from Eq. (12) and use the expansion⁴⁰

$$e^{i\mathbf{q}\cdot\mathbf{r}} = 4\pi \sum_{lm} i^l j_l(qr) Y_{lm}^*(\theta, \phi) Y_{lm}(\vartheta, \varphi),$$

where (r, θ, ϕ) and (q, ϑ, φ) are the spherical coordinates of the vectors \mathbf{r} and \mathbf{q} respectively. As a result we get

$$\begin{aligned} \mathcal{F}_{\nu\nu'}(\mathbf{q}) &= 4\pi (-1)^{m-m'} \sum_{l''=|l-l'|}^{l+l'} i^{l''} f_{ll''}^{nn'}(qR) \\ &\quad \times G_{l'l''}^{m,m-m',m'} Y_{l'',m-m'}(\vartheta, \varphi), \end{aligned} \quad (13)$$

where

$$f_{ll''}^{nn'}(u) = N_{lm} N_{l'm'} \int_0^1 dy y^2 j_{l''}(uy) j_l(x_{ln}y) j_{l'}(x_{l'n'}y)$$

and

$$\begin{aligned} G_{l'l''}^{m,m',m''} &= \int_0^{2\pi} d\phi \int_0^\pi d\theta \sin\theta \\ &\quad \times Y_{lm}^*(\theta, \phi) Y_{l'm'}(\theta, \phi) Y_{l''m''}(\theta, \phi) \end{aligned} \quad (14)$$

are Gaunt coefficients.

Using Eqs. (6), (9), and (13) we have

$$\begin{aligned} h_{\nu_1\nu_2\nu_3\nu_4}^{(\sigma_1\sigma_2\lambda\sigma_4, \text{dir})} &= \\ &\quad - \frac{4e^2 a_0}{\sqrt{3\pi} \epsilon_0 \epsilon_s R^2} \alpha_{\sigma_2\lambda} \delta_{\sigma_1, \sigma_4} \\ &\quad \times \sum_{l=|l_1-l_4|}^{l_1+l_4} \sum_{l'=|l_2-l_3|}^{l_2+l_3} i^{l-l'+1} \int_0^\infty du u f_{l_1 l_4}^{n_1 n_4}(u) f_{l_3 l_2}^{n_3 n_2}(u) \\ &\quad \times G_{l_1, l_4}^{m_1, m_1-m_4, m_4} G_{l_3, l_2}^{m_3, m_3-m_2, m_2} G_{l, l'}^{m_1-m_4, \pm 1, m_3-m_2}, \end{aligned}$$

where $\Delta m = \lambda - \sigma_2$. The $1/R^2$ dependence of the matrix element is explicit in this result. Note also that $l-l'$ must be odd for the Gaunt coefficients to be non-zero so that the matrix elements are real.

C. Surface polarization contribution

In the surface polarization-related term [Eq. (10)], we use Eq. (11) and substitute the wave functions from

Eq. (12). To reduce the product of four harmonics, we expand one pair into the Gaunt series,

$$\begin{aligned} Y_{lm}^*(\theta, \phi) Y_{1, \Delta m}(\theta, \phi) &= \\ &\quad (-1)^m \sum_{l'=|l-1|}^{l+1} G_{l'l}^{\Delta m-m, \Delta m, -m} Y_{l', \Delta m-m}(\theta, \phi). \end{aligned}$$

The resulting integrals are performed using Eq. (14). As a result, one finds

$$\begin{aligned} h_{\nu_1\nu_2\nu_3\nu_4}^{(\sigma_1\sigma_2\lambda\sigma_4, \text{pol-1})} &= \sqrt{\frac{4\pi}{3}} \frac{e^2 a_0}{\epsilon_0 \epsilon_s R^2} \alpha_{\sigma_2\lambda} \delta_{\sigma_1\sigma_4} \\ &\quad \times \sum_k \chi_k C_{k+1}^{(n_2 l_2)(n_3 l_3)} C_{k+2}^{(n_1 l_1)(n_4 l_4)} \sum_{\substack{l < k \\ l+k \text{ even}}} \sum_{l'=|l-1|}^{l+1} \\ &\quad \times G_{l_1 l_4}^{m_1, m_1-m_4, m_4} G_{l_3 l_2}^{m_3, m_3-m_2, m_2} G_{l' l_1}^{m_1-m_4, \Delta m, m_3-m_2}, \end{aligned}$$

and

$$\begin{aligned} h_{\nu_1\nu_2\nu_3\nu_4}^{(\sigma_1\sigma_2\lambda\sigma_4, \text{pol-2})} &= -\sqrt{\frac{4\pi}{3}} \frac{e^2 a_0}{\epsilon_0 \epsilon_s R^2} \alpha_{\sigma_2\lambda} \delta_{\sigma_1\sigma_4} \\ &\quad \times \sum_k \chi_k C_{k+1}^{(n_2 l_2)(n_3 l_3)} C_{k+2}^{(n_1 l_1)(n_4 l_4)} \sum_{\substack{l < k \\ l+k \text{ odd}}} \sum_{l'=|l-1|}^{l+1} \\ &\quad \times G_{l_1 l_4}^{m_1, m_1-m_4, m_4} G_{l_3 l_2}^{m_3, m_3-m_2, -m_2} G_{l' l_1}^{m_1-m_4, \Delta m, m_3-m_2}, \end{aligned}$$

where

$$C_k^{(nl)(n'l')} = N_{nl} N_{n'l'} \int_0^1 dx j_l(x_{nl}x) x^k j_{l'}(x_{n'l'}x)$$

and Δm is defined as previously. Again, these results show an explicit $1/R^2$ dependence.

IV. RESULTS

In this section, we present results of calculations performed within the simple single-band model presented above. We focus on the general statistical distribution of the coupling strengths between optically active (bright) single-exciton (X) and biexciton (BX) states vs. the energy differences between the two coupled states. This allows us to estimate the degree of mixing between the bright X and BX states. The calculations are performed for a single spherical NC with the radius $R = R_0 = 3$ nm or for a slightly inhomogeneous ensemble of NCs with the sizes given by the Gaussian distribution of their radii with the mean R_0 and the full width at half maximum (FWHM) of $\sigma = 0.3$ nm. We take $a_0 = 1.9$ nm, as estimated from the InAs parameters routinely used in $\mathbf{k} \cdot \mathbf{p}$ calculations⁴². For definiteness, we focus on the bright X states with the hole with spin projection $+3/2$ that lie in the energy range below 5 eV. This set contains 53 states in a NC of 3 nm radius (the spectrum is showed in the inset in Fig. 2(c)). The lowest BX state, which sets the energetic onset of the MEG process, is at 2.6 eV.

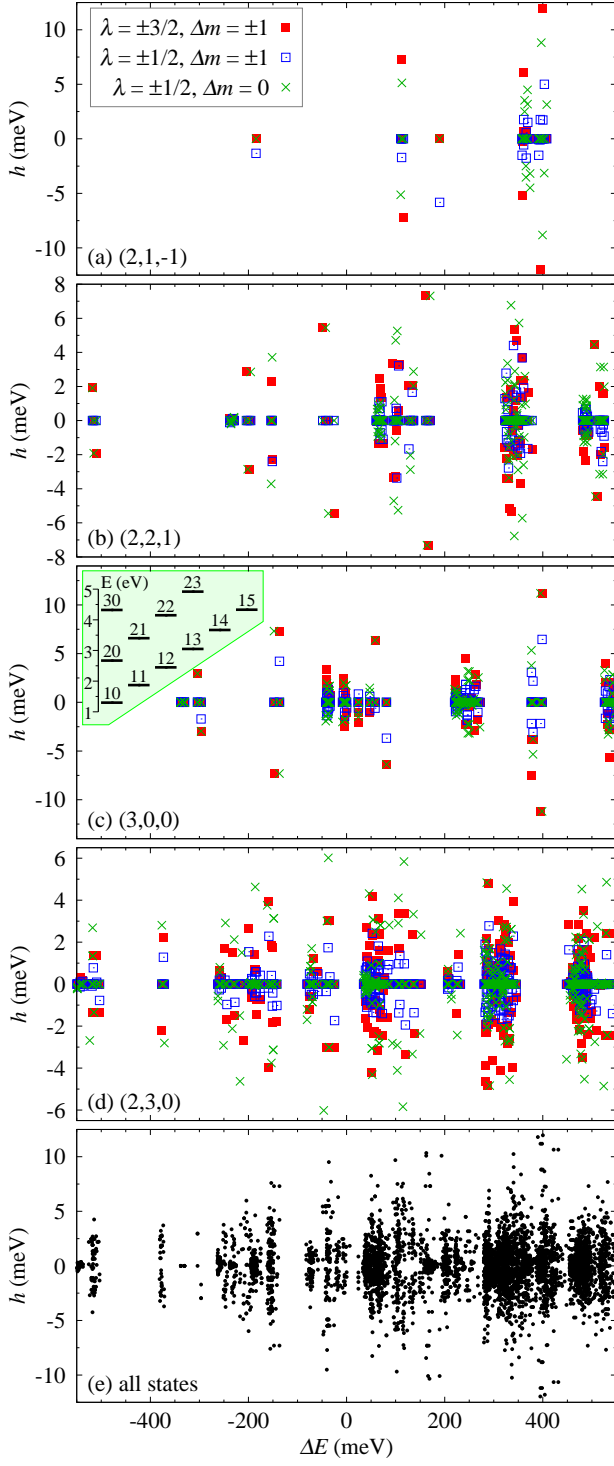


FIG. 2: (a-c) The matrix elements h between X and BX states vs. the energy distance between these states for selected X states, as shown in the labels, for a NC with the radius $R = 3$ nm. The point style encodes three groups of spin configurations of the BX state as shown in the panel (a) (see also the text). (d) The matrix elements and X-BX energy distances for all the X states below 5 eV. Inset in (c): the spectrum of the X states (the digits show the n and l values).

In order to characterize the typical X-BX Coulomb coupling strengths and the distribution of energies of the coupled BX configurations, in Fig. 2(a-c) we graphically represent these couplings for three selected bright X states (indicated by the values of the quantum numbers (n, l, m) , identical for the electron and the hole, shown in the label of each panel). Couplings to BX states within the energy interval of ± 550 meV around the energy of a given X state are shown. Each symbol corresponds to a single BX state coupled to a given X state and its position shows the energy distance from the X state and the value of the Coulomb matrix element coupling the X and BX states. The BX states are divided into three groups according to their spin configurations: 5 configurations with the spin of the newly created hole $\lambda = \pm 3/2$, 6 configurations with $\lambda = \pm 1/2$ and the envelope angular momentum change $\Delta m = \pm 1$, and 6 configurations with $\lambda = \pm 1/2$ and $\Delta m = \pm 1$. These three groups are coded into the symbol styles, as shown in the key inserted in Fig. 2(a).

One can see that typical values of the X-BX couplings are up to several meV but most of them are at most on the order of 1 meV (we have found a small number of stronger couplings, even over 30 meV, but only between energetically very distant states). There is a clear pattern in the spectral distribution of the coupled BX states which results from the shell structure of the NC spectrum. An important feature is the growing number of the coupled BX states which is consistent with the rapid growth of the overall density of BX states with increasing energy.

The features observed in the case of the three selected X states shown in Fig. 2(a-c) are confirmed by the analysis of the combined distribution for all the X states with energies below 5 eV, shown in Fig. 2(d). Altogether, there are almost 7200 BX states coupled to the 53 X states in this energy range, which is still only a tiny fraction of the total number of the BX states in this energy interval.

The results discussed above suggest that the growing number of remote BX states that are sufficiently strongly coupled to a given X state can considerably contribute to the mixing between X and BX states. Hence, a picture based on BX states in vicinity of the X state (an “energy window”) may be misleading. In order to achieve a more complete picture we have found all the states in the energy range ± 4 eV from each of the X states under consideration. This allows us to account for all the BX states for which the ratio of the X-BX matrix element h to the energy distance ΔE is greater than 0.01, except for the uncommon cases of $|h| > 40$ meV (we have not found a single instance of such a large coupling). The ratio $|h/\Delta E|$ is an important parameter as it determines (within the range of applicability of the perturbation theory) the admixture of the BX state into the X state which is crucial for the efficiency of the MEG process. In Fig. 3, we plot this ratio as a function of the energy of the X state involved. For more clarity, the results are divided

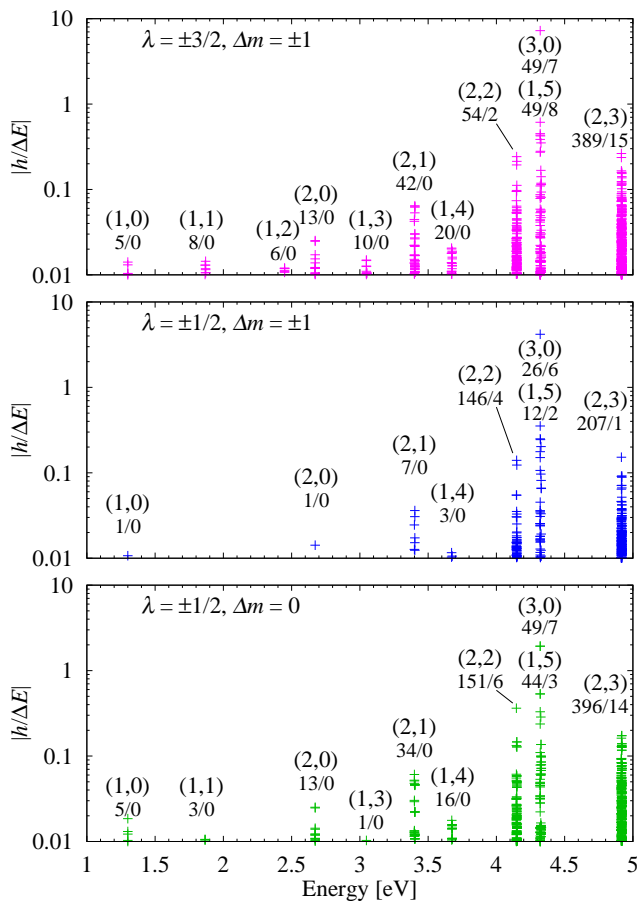


FIG. 3: The ratio of the X-BX matrix element h to the energy distance ΔE between the coupled states plotted as a function of the energy of the X state involved for a NC with the radius $R = 3$ nm. The label (n, l) indicates the quantum numbers and the label a/b shows the numbers of coupled BX states with $|h/\Delta E| > 0.01$ (a) and $|h/\Delta E| > 0.01$ (b).

into three groups according to the spin configurations of the BX state, as previously. Each “stack” of points in this figure corresponds to a set of states with fixed values of the quantum numbers n and l , as denoted in the figure (with the exception of the states $(3, 0, 0)$ and $(1, 5, m)$ which are accidentally almost degenerate for this NC size). As expected, the number of coupled BX states tends to grow with the energy of the X state which can again be attributed to the growing density of states of the BX states. As one can see, in spite of the enormous number of BX states in the energy range taken into account the number of states with $|h/\Delta E| > 0.01$ can only reach several tens for a single X state (note that the numbers in the figure give the total number of BX states coupled to all the $2l + 1$ X states). Moreover, only for a small fraction of these states one finds $|h/\Delta E| > 0.1$ (which corresponds to an admixture of BX state above 1%). For the specific NC size under study only in one case a close resonance between an X state and a coupled BX state was found that resulted in the $|h/\Delta E|$ ratio exceeding 1.

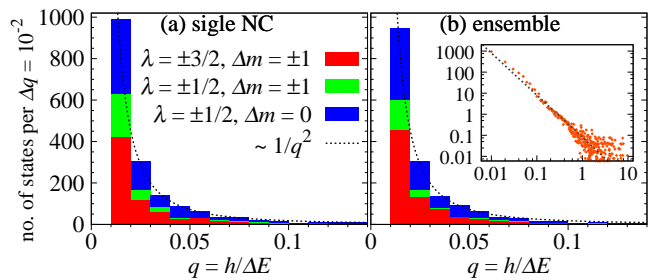


FIG. 4: Histograms of the number of coupled BX states as a function of the ratio $q = |h/\Delta E|$. The color coding represents three groups of spin configurations of the BX states and the dotted lines show a $1/q^2$ dependence. (a) A single NC with $R = 3$ nm. (b) An ensemble of NCs with the mean radius $R_0 = 3$ nm and the FWHM of the radius distribution of 0.3 nm.

Comparing the small number of states with $|h/\Delta E| > 0.01$ found in the ± 0.55 eV energy window (as shown in Fig. 2) with the much larger numbers found in the broad energy range (Fig. 3) one might conclude that remote states play an important role in the X-BX state mixing and, in consequence, in the MEG efficiency. From the point of view of theoretical modeling, this opens the critical question whether the actual situation can be reasonably approximated by a model that takes into account only BX states in a certain, sufficiently large spectral window around a given X state or, in other words, whether the approximate results converge sufficiently fast when extending the spectral window. In order to approach the answer to this question we have estimated the statistical distribution of the values of $q = |h/\Delta E|$ based on our simplified NC model. The result for a single NC with $R = 3$ nm is shown in Fig. 4(a). In order to obtain a single characteristics we present a joint distribution of the $|h/\Delta E|$ ratios for all the X states below 5 eV, divided again in the three groups of spin configurations. As could be expected, the number of weakly coupled BX states is the highest, while the number of states coupled by larger matrix elements decreases quickly with the growing strength of the coupling (note that the number of BX states in the lowest sector of q , not shown in the figure, is formally infinite). The same tendency is seen in Fig. 4(b) where an analogous distribution is shown in the same way for an ensemble of NC in which we have assumed a Gaussian distribution of the radii with the mean $R_0 = 3$ nm and the FWHM equal to 0.3 nm. In both cases, a dependence of the form $1/q^2$ is found, which is rigorously confirmed by the logarithmic plot in the inset to Fig. 4(b), where this power law dependence is seen to be maintained over a surprisingly broad range of the q values.

The fact that the exponent of this power law distribution is equal to 2 is remarkable: According to the perturbation theory (which is valid for small values of q), the admixture of a single BX state to a given X state is equal to q^2 . Hence, if there are N_q states with a certain

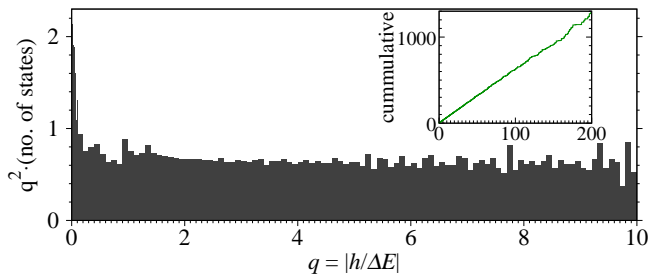


FIG. 5: Histogram of the number of coupled BX states multiplied by q^2 for an ensemble of NCs with the mean radius $R_0 = 3$ nm and the FWHM of the radius distribution of 0.3 nm.

value of q then their joint contribution is equal to $N_q q^2$. The scaling $N_q \sim 1/q^2$ means that the growing number of weakly coupling states exactly compensates the decreasing magnitude of the matrix element so that, on the average, BX states with all the coupling strengths contribute equally. This has the immediate consequence that discarding the part of the coupled states with $q < q_{\min}$ generates a computational error that decreases proportionally to q_{\min} . This means that, in principle, a numerical computation can be performed with arbitrary accuracy based on a properly selected set of BX states. In fact, since the values of the matrix elements seem to be bounded, this implies convergence in terms of the width of the energy window assumed. This property, that holds only for a power law exponent below 3, is very desirable and usually implicitly taken for granted in numerical computations^{24,25,27,35,36,43} but it seems by no means obvious.

A direct confirmation of this “homogeneous contribution” property resulting from the $1/q^2$ scaling is presented in Fig. 5. Here each histogram bar is multiplied by q^2 . As a result, a remarkably constant distribution is obtained, which is particularly visible in the inset, where the cumulative distribution is shown, which has a linear form across a very wide range of values. While this flat distribution is an interesting feature, it should be noted that the value of $q^2 N_q$ has no direct physical meaning at high q where the perturbation theory is not applicable. In fact, this part of the distribution is due to very few BX states that come to resonance with some of the X states for a certain value of R . At resonance, the value of q is infinite but the maximum admixture in the case of just two resonant states is $1/2$.

Finally, let us estimate the degree of mixing between the X and BX states. In Fig. 6, we show the BX admixture to the selected X states considered here as a function of the NC radius. This is obtained separately for each X state by diagonalizing the Hamiltonian including only the X state in question and all the BX states directly coupled to this X state by matrix elements for which $q \geq 0.01$. For each R , the eigenstate Ψ_0 with the highest X contribution is found and the BX admixture is determined

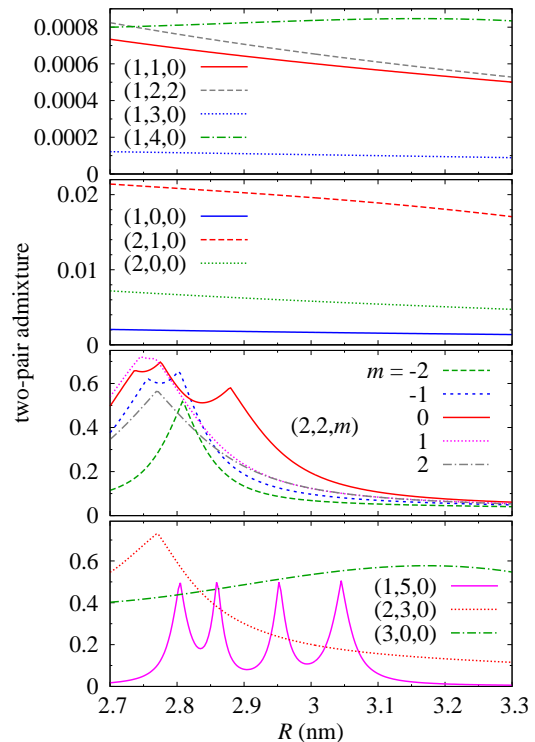


FIG. 6: Biexciton admixtures to selected exciton states.

as

$$P_{\text{BX}} = \sum_i |\langle BX_i | \Psi_0 \rangle|^2 = 1 - |\langle X | \Psi_0 \rangle|^2,$$

where $|X\rangle$ is the X state and $|BX_i\rangle$ are all the coupled BX states. We show the results for one selected state out of each subspace with fixed n and l , except for the states $(2, 2, m)$ which are presented in full to see that the admixture to states that differ only by the value of m is very similar (which is due to the fact that these states are almost degenerate).

As expected, the low energy states $(1, 0, 0)$ and $(1, 1, m)$, lying below the theoretical MEG threshold of 2.6 eV, have the BX admixtures well below 1%. However, the same is true for states lying up to 1 eV above the threshold. This property results from the selection rules that hold in the MEG process, as discussed in Sec. II: An X state needs to be located in the vicinity of a BX state to which it is coupled, which becomes likely only when the density of BX states becomes sufficiently high. On the other hand, the states with energies above 4 eV are typically much more strongly mixed with BX states. Even in these case, in spite of hundreds of BX states coupled to each such X state, the admixture only in some cases approaches 80% for a certain NC radius and for most (but not all) states drops down as R increases. Note that the admixture strongly depends on the NC size and in the case of the state $(1, 5, 0)$ shows strong oscillations. In general, while the X states are clearly not completely dissolved in the densely distributed BX states, the degree

of mixing between X and BX states becomes considerable at energies a few eV above the MEG threshold which may lead to the MEG efficiency of a few tens per cent.

V. DISCUSSION, CONCLUSIONS AND OUTLOOK

The main result presented in this paper is the method for calculating Coulomb matrix elements between exciton and biexciton states in semiconductor nanocrystals based on the envelope function formalism. We have shown that such a calculation requires proper treatment of the Bloch parts of the carrier wave functions which, in the leading order, leads to spin selection rules identical to those holding for optical interband transitions (however, the rules for envelope states are different). Moreover, the resulting matrix elements are additionally scaled by the ratio of the lattice constant to the NC radius, as compared to the usual (intraband) Coulomb couplings. As a result, the Coulomb coupling between X and BX states scale as $1/R^2$.

Once the matrix elements between single-band states are known they can be used for calculating X-BX couplings using more exact carrier states found by diagonalizing the 8-band Kane ($\mathbf{k} \cdot \mathbf{p}$) Hamiltonian. This approach has been found to correctly reproduce the NC spectrum down to very small sizes⁴⁴ and, when combined with the results presented here, can provide quantitatively accurate description of the MEG process in NCs. For more accuracy, Coulomb correlations, in particular in BX states³⁵, could also be included. While atomistic models may offer more accurate single particle wave functions and allow one to include more system features (e.g., surface defects⁴⁵), their high computational costs limits the extent to which few-particle states and couplings between them can be treated. Typically, when following an atomistic approach, one is forced to restrict the calculations to an energy window around a given X or BX state and to truncate the basis of BX states when simulating the system dynamics³⁵. From this point of view, the method based on the envelope function formalism may offer a complementary approach to the trade-off between the accuracy of single-particle states and the reliability of few-particle modeling in which the accuracy

of the atomistic models is sacrificed in favor of lowering the computational effort, which offers considerably more flexibility on the subsequent stages of theoretical analysis, including the system dynamics^{35,36} and dissipative evolution^{31,32,37,38}, where finding the X-BX coupling is the essential prerequisite for further modeling. An additional benefit is the transparent nature of our envelope function method, which offers mostly analytical treatment and does not rely on large computational resources or dedicated software, hence can easily be employed by a broad community of researchers.

While performing full multi-band $\mathbf{k} \cdot \mathbf{p}$ calculations is beyond the scope of this work, we have presented some preliminary estimates of the statistical distribution of the coupling magnitudes and the energies of the coupled states using a very simple single-band envelope function approach. Such overall statistical conclusions are likely to be valid even if the underlying characteristics of individual states are not absolutely accurate. We have shown that the number of BX states coupled to X states form a certain energy range scales as inverse square of the ratio of the coupling magnitude to the energy separation. This scaling property is remarkable as it guarantees that the contribution of remote states is finite and controllable, which justifies limiting the computation to an energy window (no matter what computational method is chosen)^{24,25,27,35,36,43}.

Finally, we have estimated the degree of mixing between X and BX states as a function of the NC size. Very small BX admixture to X states has been found below and within 1 eV above the MEG threshold. Much larger mixing, reaching 80%, appears for higher-energy states. The amount of BX admixture to this states varies quite strongly when the NC radius is changed by a fraction of a nanometer. This may suggest that modeling based on a single NC size may not be representative for average properties of an ensemble.

Acknowledgments

This work was supported in part by the TEAM programme of the Foundation for Polish Science, co-financed from the European Regional Development Fund.

¹ A. J. Nozik, *Physica E* **14**, 115 (2002).

² R. D. Schaller, V. M. Agranovich, and V. I. Klimov, *Nat. Phys.* **1**, 189 (2005).

³ V. I. Rupasov and V. I. Klimov, *Phys. Rev. B* **76**, 125321 (2007).

⁴ R. D. Schaller and V. I. Klimov, *Phys. Rev. Lett.* **92**, 186601 (2004).

⁵ R. Ellingson, M. Beard, J. Johnson, P. Yu, O. Micic, A. Nozik, A. Shabaev, and A. Efros, *Nano Lett.* **5**, 865 (2005).

⁶ R. Schaller, J. Pietryga, and V. Klimov, *Nano Letters* **7**,

3469 (2007).

⁷ J. J. H. Pijpers, E. Hendry, M. T. W. Milder, R. Fanciulli, J. Savolainen, J. L. Herek, D. Vanmaekelbergh, S. Ruhman, D. Mocatta, D. Oron, A. Aharoni, U. Banin, and M. Bonn, *J. Phys. Chem. C* **111**, 4146 (2007).

⁸ M. C. Beard, K. P. Knutsen, P. Yu, J. M. Luther, Q. Song, W. K. Metzger, R. J. Ellingson, and A. J. Nozik, *Nano Lett.* **7**, 2506 (2007).

⁹ M. Ji, S. Park, S. T. Connor, T. Mokari, Y. Cui, and K. J. Gaffney, *Nano Lett.* **9**, 1217 (2009).

- ¹⁰ M. T. Trinh, R. Limpens, W. D. A. M. de Boer, J. M. Schins, L. D. A. Siebbeles, and T. Gregorkiewicz, *Nature Photonics* **6**, 316 (2012).
- ¹¹ R. D. Schaller, M. Sykora, J. M. Pietryga, and V. I. Klimov, *Nano Lett.* **6**, 424 (2006).
- ¹² G. Nair and M. Bawendi, *Phys. Rev. B* **76**, 081304 (2007).
- ¹³ M. T. Trinh, A. J. Houtepen, J. M. Schins, T. Hanrath, J. Piris, W. Knulst, A. P. L. M. Goossens, and L. D. A. Siebbeles, *Nano Lett.* **8**, 1713 (2008).
- ¹⁴ J. J. H. Pijpers, E. Hendry, M. T. W. Milder, R. Fanciulli, J. Savolainen, J. L. Herek, D. Vanmaekelbergh, S. Ruhman, D. Mocatta, D. Oron, A. Aharoni, U. Banin, and M. Bonn, *J. Phys. Chem. C* **112**, 4783 (2008).
- ¹⁵ M. Ben-Lulu, D. Mocatta, M. Bonn, U. Banin, and S. Ruhman, *Nano Lett.* **8**, 1207 (2008).
- ¹⁶ G. Nair, S. M. Geyer, L.-Y. Chang, and M. G. Bawendi, *Phys. Rev. B* **78**, 125325 (2008).
- ¹⁷ J. A. McGuire, J. Joo, J. M. Pietryga, R. D. Schaller, and V. I. Klimov, *Accounts Chem. Res.* **41**, 1810 (2008).
- ¹⁸ J. A. McGuire, M. Sykora, J. Joo, J. M. Pietryga, and V. I. Klimov, *Nano Lett.* **10**, 2049 (2010).
- ¹⁹ D. J. Binks, *Phys. Chem. Chem. Phys.* **13**, 12693 (2011).
- ²⁰ J. B. Sambur, T. Novet, and B. A. Parkinson, *Science* **330**, 63 (2010).
- ²¹ O. E. Semonin, J. M. Luther, S. Choi, H.-Y. Chen, J. Gao, A. J. Nozik, and M. C. Beard, *Science* **334**, 1530 (2011).
- ²² K. Hyeon-Deuk and O. V. Prezhdo, *Nano Lett.* **11**, 1845 (2011).
- ²³ K. Hyeon-Deuk and O. V. Prezhdo, *ACS Nano* **6**, 1239 (2012).
- ²⁴ A. Franceschetti, J. M. An, and A. Zunger, *Nano Lett.* **6**, 2191 (2006).
- ²⁵ E. Rabani and R. Baer, *Nano Lett.* **8**, 4488 (2008).
- ²⁶ M. Califano, *ACS Nano* **3**, 2706 (2009).
- ²⁷ R. Baer and E. Rabani, *Nano Lett.* **12**, 2123 (2012).
- ²⁸ G. Allan and C. Delerue, *Phys. Rev. B* **73**, 205423 (2006).
- ²⁹ C. Delerue and G. Allan, *Phys. Rev. B* **81**, 125306 (2010).
- ³⁰ M. Korkusinski, O. Voznyy, and P. Hawrylak, *Phys. Rev. B* **82**, 245304 (2010).
- ³¹ A. Shabaev, A. L. Efros, and A. J. Nozik, *Nano Lett.* **6**, 2856 (2006).
- ³² W. Witzel, A. Shabaev, C. Hellberg, V. Jacobs, and A. Efros, *Phys. Rev. Lett.* **105**, 137401 (2010).
- ³³ L. Silvestri and V. M. Agranovich, *Phys. Rev. B* **81**, 205302 (2010).
- ³⁴ A. L. Efros and M. Rosen, *Phys. Rev. B* **58**, 7120 (1998).
- ³⁵ M. Korkusinski, O. Voznyy, and P. Hawrylak, *Phys. Rev. B* **84**, 155327 (2011).
- ³⁶ E. Rabani and R. Baer, *Chem. Phys. Lett.* **496**, 227 (2010).
- ³⁷ A. Piryatinski and K. A. Velizhanin, *J. Chem. Phys.* **133**, 084508 (2010).
- ³⁸ K. A. Velizhanin and A. Piryatinski, *Phys. Rev. Lett.* **106**, 207401 (2011).
- ³⁹ L. E. Brus, *J. Chem. Phys.* **80**, 4403 (1984).
- ⁴⁰ J. Jackson, *Classical electrodynamics* (Wiley, New York, 1998).
- ⁴¹ T. Takagahara, *Phys. Rev. B* **47**, 4569 (1993).
- ⁴² P. Y. Yu and M. Cardona, *Fundamentals of Semiconductors*, 3 ed. (Springer, Berlin, 2005).
- ⁴³ G. Allan and C. Delerue, *Phys. Rev. B* **77**, 125340 (2008).
- ⁴⁴ U. Banin, C. J. Lee, A. A. Guzelian, A. V. Kadavanich, A. P. Alivisatos, W. Jaskolski, G. W. Bryant, A. L. Efros, and M. Rosen, *J. Chem. Phys.* **109**, 2306 (1998).
- ⁴⁵ H. M. Jaeger, S. Fischer, and O. V. Prezhdo, *J. Chem. Phys.* **136**, 064701 (2012).